Assessing the Accuracy of a Linearized Observation Operator for Assimilation of Radio Occultation Data: Case Simulations with a High-Resolution Weather Model

SERGEY SOKOLOVSKIY

University Corporation for Atmospheric Research, Boulder, Colorado, and A. M. Obukhov Institute of Atmospheric Physics, Moscow, Russia

YING-HWA KUO

University Corporation for Atmospheric Research, and National Center for Atmospheric Research, Boulder, Colorado

WEI WANG

National Center for Atmospheric Research, Boulder, Colorado

(Manuscript received 30 December 2003, in final form 3 December 2004)

ABSTRACT

Assimilation into numerical weather models of the refractivity, Abel-retrieved from radio occultations, as the local refractivity at ray tangent point may result in large errors in the presence of strong horizontal gradients (atmospheric fronts, strong convection). To reduce these errors, other authors suggested modeling the Abel-retrieved refractivity as a nonlocal linear function of the 3D refractivity, which can be used as a linear observation operator for assimiliation. The authors of this study introduce their approach for the nonlocal linear observation operator, which consists of modeling the excess phase path, calculated along certain trajectories below the top of an atmospheric model. In this study (not aimed at development of an observation operator for any specific atmospheric model), both approaches are validated by assessing the accuracy of both linearized observation operators by numerical simulations with the high-resolution Weather Research and Forecasting (WRF) model and comparing them to the accuracy of interpretation of the Abel-retrieved refractivity as local. Improvement of the accuracy of about an order of magnitude is found with the nonlocal refractivity and further improvement is found with the excess phase path. The effect of horizontal resolution of an atmospheric model on the accuracy of modeling local and nonlocal linear observables is also investigated, and it is demonstrated that the nonlocal linear modeling of radio occultation observables is especially important for weather prediction models with sufficiently high horizontal resolution, grid size <100 km (mesoscale models).

1. Introduction

Radio occultation (RO) remote sensing of the atmosphere includes transmission and reception of coherent radio signals propagating through the atmosphere between satellites, such as the global positioning system (GPS) and low earth-orbiting (LEO) satellites (Gurvich and Krasil'nikova 1987; Yunck et al. 1988, 2000; Hardy et al. 1992; Melbourne et al. 1994; Hocke 1997; Kursinski et al. 1997, 2000; Rocken et al. 1997; Steiner et al. 1999; Feng and Herman 1999; Syndergaard 1999; Anthes et al. 2000; Wickert et al. 2001; Hajj et al. 2002). Refraction of radio waves in the atmosphere affects the phase and amplitude of radio signals. The acquired complex RO signal, first, is used for reconstruction of the bending angle of a ray as the function of impact parameter, under the assumption of local spherical symmetry of refractivity. Next, this function is inverted into the refractivity as the function of radius (Abel inversion). The refractivity is related to pressure, temperature, and humidity (Thayer 1974), the common meteorological variables used in numerical weather prediction (NWP) models. Reconstruction of these variables from refractivity, for use in NWP models, needs the use of ancillary data. Alternatively, the refractivity or the bending angle profiles can be directly

Corresponding author address: Sergey Sokolovskiy, 3300 Mitchell Ln., #3436, Boulder, CO, 80301.
E-mail: sergey@ucar.edu

assimilated, as the observables, by NWP models (Eyre 1994; Zou et al. 1995, 1999, 2000; Kuo et al. 2000; Liu et al. 2001; Poli et al. 2002; Liu and Zou 2003; Marquardt et al. 2003; Gorbunov and Kornblueh 2003). Then these profiles (vectors) must be supplied with the corresponding observation operators (commonly called the forward model), which provides mapping from the model space to the observation space. The most common and simple approach is to assimilate the Abel-retrieved (AR) refractivity as the local refractivity at the estimated tangent point (TP) of a ray. This approach may work fairly well in the absence of strong horizontal refractivity gradients. In the troposphere, especially in case of atmospheric fronts, hurricanes, strong convection, etc., the horizontal gradients of refractivity may introduce significant errors. The errors due to horizontal gradients have been modeled by, for example, Gurvich and Sokolovsky (1985), Sokolovsky (1986), Gorbunov and Sokolovskiy (1993), Gorbunov et al. (1996), Kursinski et al. (1997), Ahmad and Tyler (1999), and recently by Syndergaard et al. (2003, 2005), Poli and Joiner (2004), and Poli (2004). In most of the studies, they use either analytical or global atmospheric models. Kursinski et al. (1997) give an estimate of rms refractivity error in the lower troposphere of about 1 N unit. With a high-resolution model, such as the one used in this study, these errors can be significantly larger. To reduce these errors, the bending angle or the AR refractivity must be modeled with account for the horizontal gradients reproduced by NWP model fields.

Because of the dependence of ray trajectory on the refractivity, the observed phase and the derived bending angle are nonlinear functions of the 3D refractivity (the corresponding observation operators are nonlinear). These functions can be linearized by fixing ray trajectories (which then do not depend on the refractivity). However, the accuracy of the linearization (and of the corresponding linear operator), in certain cases, may be insufficient in the troposphere where deviation of true ray trajectories from those used as the background for the linearization is significant. In those cases accurate modeling of the RO observables from NWP model fields may require iterations where the ray trajectories are adjusted at each step. This approach, applied for modeling of the observation bending angle profiles, is discussed by, for example, Eyre (1994), Zou et al. (2000), Gorbunov and Kornblueh (2003), and Poli and Joiner (2005).

Linearization of the forward modeling and inverting RO observations in earth's atmosphere was considered, for example, by Gorbunov (1990) and later by Ahmad (1998) and Ahmad and Tyler (1998). When modeling of an RO observable includes forward and inverse modeling, and the same fixed model of ray trajectory is used at both steps, this results in substantial cancellation (reduction) of the errors related to linearization. This approach, outlined by Ahmad (1998) and Ahmad and Tyler (1998), was applied by Syndergaard et al. (2003) for nonlocal linear modeling ("2D mapping") of the AR refractivity. In this approach, a fairly reasonable accuracy can be achieved by use of a relatively simple model of ray trajectories, for example, straight lines, without the iterations. This allows development of a relatively simple and computationally fast linear observation operator. An additional advantage of this approach, in the form applied by Syndergaard et al. (2003), is that it allows modeling of the AR refractivity below the top of an NWP model without the use of ancillary information above the top (which is required for modeling of the observation bending angles).

Recently, other studies related to development of nonlocal linear observation operators have been completed. Syndergaard et al. (2005) present detailed description of the nonlocal refractivity observation operator (2D mapping) outlined in their earlier study (Syndergaard et al. 2003) and generalize their approach by introducing curvature of ray trajectories and considering mapping alternatively on geometric height levels or on pressure levels. Poli (2004), in particular, considers a linear observation operator for the bending angle by integrating a vertical component of the refractivity gradient along some precalculated ray trajectory. The operators introduced in the referenced studies and in this study are similar in the sense that they model RO observables by integrating 2D (3D) refractivity (or its gradient) along some fixed trajectories that do not depend on this refractivity, thus resulting in significant computational savings.

In this study we follow the approach outlined by Ahmad (1998) and Syndergaard et al. (2003) in the sense that we linearize the forward model by fixing the ray trajectory. But we modify the referenced approach by introducing the excess phase path, integrated along a certain model of ray trajectory below the top of an NWP model, through the AR refractivity, as the new observable instead of the AR refractivity. Linear modeling of this new observable consists of integrating the excess phase path along exactly the same ray trajectory through the 3D refractivity represented by an NWP model or analysis. Similarly to the nonlocal linear modeling of the AR refractivity (see above), the errors related to linearization are canceled to a considerable extent when using the excess phase path as the observable. This is due to the use of the same fixed model of ray trajectory for obtaining this observable from the 1D

AR refractivity and for modeling this observable from the 3D NWP model or analysis refractivity. We introduce a model of the fixed ray trajectory for the linearization, which yields improvement compared to the straight line and is fairly simple for practical implementation. In this study, which is not aimed at development of an observation operator for a specific model and data assimilation system, we only consider 2D occultations (in one plane) and we use the 2D refractivity as the state vector, without considering mapping of this vector to the true NWP state vector represented by model variables (which can be different for different NWP models).

Next, we evaluate the linearized observation operators by numerical simulations with the high-resolution Weather Research and Forecasting (WRF) model. In this study we use two cases: the atmospheric front (which triggered strong convection uprising to the tropopause) over the southeastern United States on 11 November 2002 and Hurricane Isabel over the Atlantic, which hit the east coast of the United States on 17 September 2003. The simulations show reduction of the observation errors (defined at the end of this section) when modeling the AR refractivity as the nonlocal refractivity and further, when using the excess phase as the observable. Additionally, we demonstrate the effect of horizontal resolution of an atmospheric model on the observation errors when modeling the AR refractivity as local and nonlocal refractivities.

Section 2 describes linearization of two observation operators. Section 2a gives an overview of the linearization of the AR (nonlocal) refractivity following Ahmad (1998) and Syndergaard et al. (2003). Section 2b introduces our approach for linearization of the excess phase path and its usage as the new observable. Section 3 describes the high-resolution WRF model used in the simulations. Section 4 discusses some details of the numerical simulations used in this study. Section 5 presents the results of the simulations, and section 6 concludes the study.

In this paper we adhere to the following definition of errors. Observation error is the apparent difference between a physical quantity (observable) obtained from observations and modeled by use of an atmospheric model. The observation errors include the modeling errors, the representativeness errors, and the measurement errors. Modeling errors are the errors related to approximations applied for modeling of an observable. For example, in this study, treating the AR refractivity as local introduces the modeling error. Representativeness errors are the errors related to discrete representation of continuous meteorological fields by an atmospheric model. The measurement errors are related to the physical processes that affect observations but may not be modeled in the deterministic sense (e.g., effect of the atmospheric turbulence and the ionospheric irregularities). The measurement errors are not considered in this study.

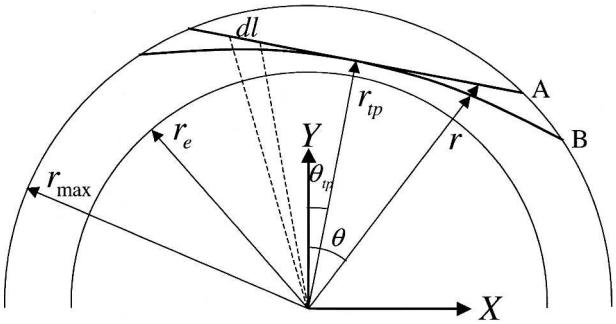

FIG. 1. Layout of ray trajectories for modeling of nonlocal, linearized RO observables: A is the straight line, and B is an arbitrary model of ray trajectory.

2. Linearization of the observation operators

a. *Linearization of the Abel-retrieved (nonlocal) refractivity*

Here we briefly outline the approach for approximation of the AR refractivity as linear function of the 3D refractivity field introduced by Ahmad (1998) and applied by Syndergaard et al. (2003). The geometry and the necessary notations are shown in Fig. 1.

Let S be the excess phase path along an arbitrary trajectory below the top of an NWP model:

$$S = \int \nu(x, y)dl, \tag{1}$$

where $\nu(x, y) = 1 - n(x, y)$, n is the 2D refractive index in the occultation plane (transmitter - receiver - center of sphericity) and $N = 10^6\nu$ is the refractivity. The trajectory introduced above is used as the model of ray with radius of TP, r_{tp}. There is certain freedom in defining this trajectory. Most important, this trajectory must not depend on $n(x, y)$, thus resulting in linearization of the problem. In a special case, when this trajectory is the ray in some background 1D refractive index $n_{\text{bg}}(r)=1+\nu_{\text{bg}}(r)$, the expression (1) can be explicitly written as

$$S(a) = 2\int_a^{a_{\max}} \frac{\nu(x, y)(1 - \rho d \ln n_{\text{bg}}/d\rho)}{n_{\text{bg}}(\rho)\sqrt{\rho^2 - a^2}}\rho d\rho, \tag{2}$$

where $\rho = rn_{\text{bg}}(r)$ is the refractional radius, and $a = r_{\text{tp}}n_{\text{bg}}(r_{\text{tp}})$ is the impact parameter. If one assumes that

$\nu(x, y) = \nu(\rho)$, then (2) can be inverted [solved with respect to $\nu(\rho)$] by use of the Abel transform:

$$\nu(\rho) = -\frac{n_{bg}(\rho)}{\pi(1 - \rho d \ln n_{bg}/d\rho)} \int_{\rho}^{\rho_{max}} \frac{dS/da}{\sqrt{a^2 - \rho^2}} da. \tag{3}$$

According to (2)–(3), $n(\rho) = 1 + \nu(\rho)$ is the nonlocal linear function of the 2D refractive index $n(x, y)$, which can be interpreted as the nonlocal linear model $n_{mod}(\rho)$ of the AR refractive index $n_{ar}(\rho)$. Alternative forms of this function, expressed through series expansions and special functions, were derived by Gorbunov (1990) and Ahmad (1998). Syndergaard et al. (2003) used the $n_{bg} = 1$, by introducing $n_{mod}(\rho) = n_{mod}(r)$ as the 2D-mapped refractive index. Generally, one can use as the $n_{bg}(\rho)$ any spherically symmetric refractive index that approximately reproduces mean atmospheric state, in particular, $n_{ar}(\rho)$. We note that the Abel inversion (3) differs from the common Abel inversion in two respects: (i) the ray trajectory does not depend on $n(x, y)$ and (ii) the upper limit of integration is finite, providing finite value $\nu_{mod}(\rho_{max})$ because $dS/da \to \infty$ when $a \to a_{max}$. Thus the extension of an NWP model state vector $\nu(x, y)$ beyond the top of the model grid is not needed for modeling of the AR refractivity as the nonlocal linear function. However, when $\rho \to \rho_{max}$ the integration path tends to zero and the information about horizontal N gradients vanishes in the nonlocal refractivity; that is, $\nu(\rho)$ simply converges to local value $\nu(x, y)$. Thus the use of the nonlocal refractivity is advantageous (effectively accounts for the horizontal N gradients) at $\rho < \rho_{max} - H$, where H is the vertical atmospheric scale (typically ~6–8 km).

For preliminary estimation of the observation errors, when modeling the AR refractivity as the nonlocal linear function of the 2D refractivity, we use an idealized model of atmospheric front (more realistic simulations are presented in the following sections):

$$\nu(z, \theta) = \nu_0 \exp(-z/H)[1 + \mu f((z/\epsilon - r_e\theta)/d)], \tag{4}$$

where $z = r - r_e$ is height, $r_e = 6370$ km is the earth's radius, $r = \sqrt{x^2 + y^2}$, $\theta = \arctan(x/y)$ is central angle, $\nu_0 = 3 \times 10^{-4}$, $H = 7.5$ km, $\epsilon = 0.03$, $d = 50$ km, and $\mu = 0.1$. The function $f(\xi) = \sin(\pi\xi/2)$ for $\xi \lesseqgtr \pm 1$ and $f(\xi) = \pm 1$ for $\xi \gtreqless \pm 1$. The parameters ϵ, d, and μ define the slope of the frontal zone with respect to earth's surface, the horizontal half-width of the frontal zone, and the fractional half-lapse of refractivity across the frontal zone.

The refractivity model (4) was subject to ray tracing (details provided in section 4). Both the bending angle α and the impact parameter a were calculated from ray arrival angle at receiver (obtained by ray tracing) under the assumption of spherical symmetry. The function $\alpha(a)$ was subject to Abel inversion. The central angle θ_{tp} of ray TP for a given r_{tp} was calculated, also, under the assumption of spherical symmetry (see section 4). Then $S(r_{tp})$ was calculated by (2), by specifying the central angle θ_{tp} for each straight line according to the estimated $\theta_{tp}(r_{tp})$. The calculated $S(r_{tp})$ was inverted into $n_{mod}(r)$ by use of (3).

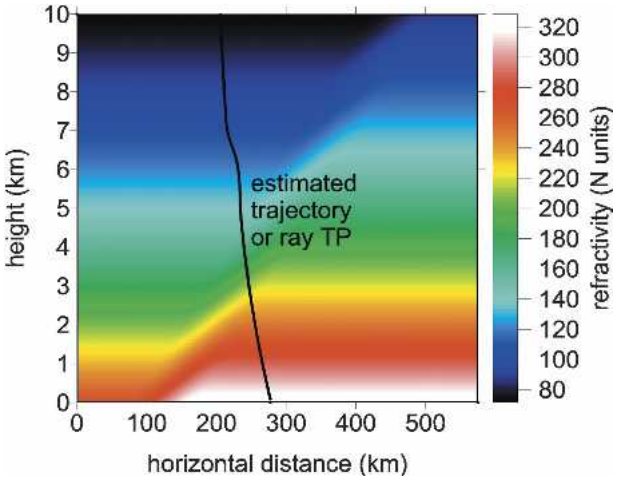

FIG. 2. Two-dimensional refractivity for the model of atmospheric front (color scale), and the estimated trajectory of ray tangent points during the occultation (black line).

Figure 2 shows the refractivity introduced by the model of atmospheric front (4) (by color scale) and the trajectory of ray TP (by solid line) estimated for the occultation geometry used in the simulations.

Figure 3 (left panel) shows (line A) the Abel retrieved refractivity $N_{ar}(z)$; (line B) the local 2D refractivity at the estimated ray TP, $N_{loc}[z, \theta_{tp}(z)]$; and (line C) the nonlocal refractivity $N_{mod}(z)$ modeled by use of the straight lines. Figure 3 (right panel) shows fractional differences: (line B) $(N_{loc} - N_{ar})/N_{ar}$ and (line C) $(N_{mod} - N_{ar})/N_{ar}$. As seen, in the presence of strong horizontal gradients, the AR and the local refractivities differ significantly, while the nonlocal linear modeling of the refractivity, by use of straight lines as the models of rays, reduces the differences by approximately an order of magnitude.

b. *Linearization of the phase path and its usage as the observable*

The nonlocal linear modeling of the AR refractivity includes two steps: forward [Eq. (2)] and inverse [Eq. (3)] modeling. In this study we are suggesting an alter-

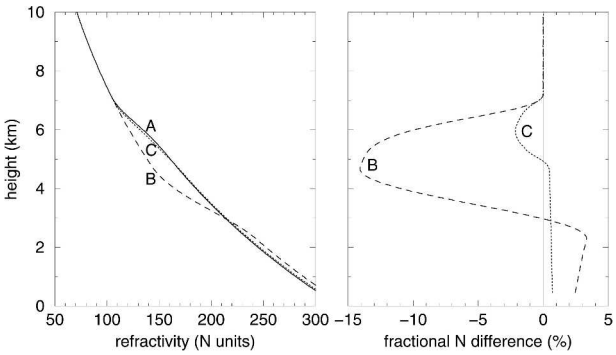

FIG. 3. Comparison of the refractivities. (left) Line A is AR refractivity, B is local refractivity at the estimated TP, and C is the nonlocal refractivity (integration along straight lines). (right) Fractional differences between the local and the AR refractivities (line B) and between the nonlocal and the AR refractivities (line C).

native approach for assimilation of RO data that consists of only the use of the forward model. The excess phase path [Eq. (1)] integrated below the top of an NWP model through 1D AR refractive index $n_{ar}(r)$ along certain fixed trajectories symmetric with respect to θ_{tp} for each r_{tp} (these trajectories are the models of rays) is considered as the new observable S_{obs} (r_{tp}). Then the excess phase path integrated along exactly the same fixed trajectories through the NWP model refractive index $n(x, y)$ is the modeled observable S_{mod} (r_{tp}). We note that the new introduced observable, whose magnitude ranges from about 1 m at 30–35 km to about several hundred meters at the surface, must not be compared and is not directly related to the true RO excess phase, because it does not use the true ray trajectory. The linear Eq. (1) in discrete representation $S_i = O_{i\{k\}}\nu_{\{k\}}$ defines the matrix $O_{i\{k\}}$ of the observation operator. Index i is associated with ith ray, while index $\{k\}$, in fact, is the set of indices identifying the NWP model grid cells. The matrix of the observation operator $\mathbf{O}$ depends on (i) the model grid; (ii) the position of the occultation plane for each ray (defined by latitude and longitude of TP, and by azimuth); and (iii) the model of ray trajectory used for the integration of the phase. For example, in the case of voxel representation of the NWP model refractivity, $O_{i\{k\}}$ is simply the length of ith ray trajectory inside the $\{k\}$th NWP model voxel. However, pixel representation with interpolation (see section 4) generally provides better accuracy.

The excess phase observation operator is a nonlocal linear operator that allows simple numerical implementation. The finite-difference representation of the numerical integration can be fairly arbitrary, but, most important, it must be the same for both $n(x, y)$ and $n_{ar}(r)$, thus resulting in cancellation, to a considerable extent, of the modeling errors. Typically, vertical resolution of RO is higher than that of most NWP models. Thus, prior to the integration, it is necessary to apply smoothing (variable with height) and resampling of the AR refractivity in order to make its vertical resolution and discretization consistent with those of the NWP model (see also section 5).

The excess phase observation operator is a smoothing operator with respect to the AR refractivity. However, it does not suppress the high-frequency content of RO observation beyond the level available in the original RO observable, which is the phase (although different from the modeled one). The error covariance E_s of the modeled phase can be readily obtained from the error covariance E_N of the AR refractivity by use of the forward operator $\mathbf{O}$ given by (2) [where $\nu(x, y)$ is set to $\nu(r)$], $E_S = \mathbf{O}E_N\mathbf{O}^T$ (where ^{T} means transpose). With thus obtained error covariance, assimilation of the nonlocal refractivity and excess phase must be equivalent since they result in the same cost function, as shown by Syndergaard et al. (2004, manuscript submitted to *Proc. OPAC-2 Int. Workshop*). However, when iterations are needed for minimization of the cost function, the use of excess phase as the observable will result in smaller number of operations. This is because at each iteration it is sufficient to only calculate the phase from an atmospheric model, but not to invert it (the inversion is necessary for the nonlocal refractivity). On the other side, calculation of the phase from the AR refractivity is performed only once.

Similarly to the nonlocal refractivity, the information about horizontal N gradients vanishes in the excess phase when TP is close to the top of atmospheric model. Thus the use of the $S(a)$ is advantageous at $a < a_{max} - H$ where H is the vertical atmospheric scale.

In this study, besides the straight line $r(\theta) = r_{tp}/\cos(\theta - \theta_{tp})$, we consider the following simple model of ray trajectory for calculation of the excess phase path:

$$r(\theta) = r_{tp}[1 + (1 - r_{tp}/r_c)(\theta - \theta_{tp})^2/2]. \qquad (5)$$

Expression (5) is the first-order expansion, in terms of small parameter $(\theta - \theta_{tp})^2$, of the equation of circle of radius r_c tangent to straight line at TP. The radius r_c must depend on r_{tp}.

Figure 4 compares the excess phase paths S_{mod} (r_{tp}), obtained by integration through the 2D model of atmospheric front (4) $n(x, y)$, and S_{obs} (r_{tp}), obtained by integration through the 1D AR refractive index n_{ar} (r). Only fractional differences $(S_{mod} - S_{obs})/S_{obs}$ are shown. Curve A was obtained by use of straight lines for integration of the excess phase path. Curve B was obtained by use of ray trajectories given by (5) when r_c was equal to ray curvature radius at TP $r_c = -n_{ar}$ (r_{tp}) $(dn_{ar}/dr_{tp})^{-1}$.

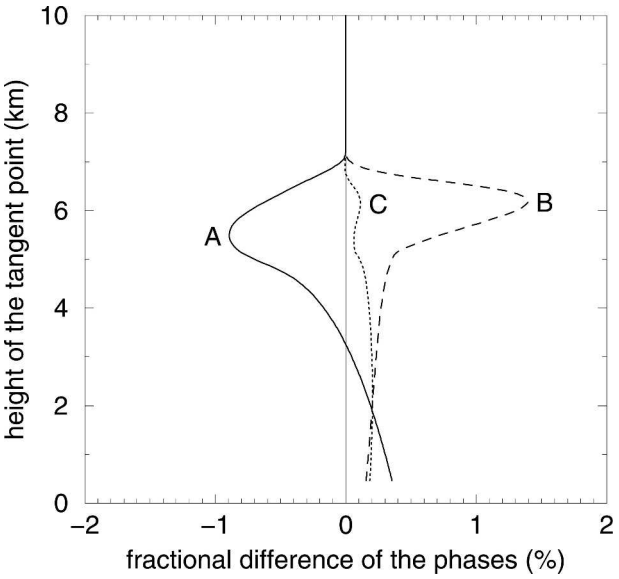

FIG. 4. Fractional difference between the excess phase paths in the 2D model and in the 1D AR refractivities. Different curves correspond to different models of ray trajectories (for details see text).

Although one could expect improvement (reduction of the modeling errors) by accounting for ray curvature at TP, curve B does not show an improvement. This is because the curvature of real ray decreases with increasing distance from TP. To account for this effect, the r_c in (5) must be taken larger than at TP. Curve C was obtained by use of a simple ad hoc model for r_c:

$$r_c = r_{c0} \exp[(r_{\text{tp}} - r_e)/h_0], \tag{6}$$

with the parameters $r_{c0} = 25000$ km, $h_0 = 6$ km, resulting in significantly smaller errors compared to the use of straight lines (curve A). Along with the straight-line model, the ray model [(5)–(6)] will be used in numerical simulations with the high-resolution WRF model described in the following sections.

3. High-resolution model simulations of mesoscale weather systems

The weather model used in this study is the WRF model (Skamarock et al. 2001; Michalakes et al. 2001), a nonhydrostatic, fully compressible, primitive equation model. It uses a terrain-following hydrostatic pressure coordinate and the Arakawa C grid staggering. The version of the model used in this study has the horizontal grid size of 4 km and 34 levels in the vertical from the surface to about 20 km. The physics of the model includes the Purdue Lin microphysics scheme (Lin et al. 1983; Chen and Sun 2002), Yosei University planetary boundary layer (PBL) scheme, University of Oregon land surface model, Rapid Radiative Transfer Model longwave radiation, and Dudhia shortwave radiation scheme. The WRF model is used to perform simulations of two significant weather events.

The first event is a frontal convection case. In this case, a strong surface front passed through the eastern United States and triggered severe convection (including large hail and tornadoes) ahead of the front from Mississippi, Alabama, and Georgia to Tennessee, Kentucky, and Ohio. The WRF model with a mesh size of 381×381 was initialized at 1200 UTC 10 November 2002 and run for 24 h to cover the initiation and strong convective period. The data used for the observation operator study were extracted from a cross section perpendicular to the surface front at 12-h forecast time. For this case, the initial condition was obtained from the National Centers for Environmental Prediction (NCEP) Eta Model 40-km operational analysis, and the lateral boundary conditions were obtained from the Eta operational forecasts provided at 40-km resolution and 3-h intervals.

The second case, Hurricane Isabel, was initialized from the Global Forecast System (GFS) operational analysis provided at 1° resolution. The lateral boundary conditions were obtained from the operational GFS forecast at 6-h intervals. Hurricane Isabel formed over the Atlantic Ocean on 7 September 2003 and remained a category 4 and 5 hurricane between 9 and 15 September. The storm was then weakened to a category 2 hurricane before it made landfall at 1700 UTC 18 September. The 4-km WRF model forecast with a mesh size of 501×501 was initialized at 0000 UTC 17 September 2003 and run for 48 h. The WRF model simulated the storm track and the timing of landfall with high accuracy. The model data, used for assessing the accuracy of the linearized observation operator in this study, were taken from a north–south cross section cutting through the center of the hurricane at 24-h forecast time.

4. Numerical implementation of the simulations

In this simulation study the WRF model 3D grid fields were initially interpolated to the selected occultation plane with constant increment in θ. The refractive index $n = 1 + \nu$, at first, was calculated in the model grid points $\nu_{i,j} = \nu(z_{ij}, \theta_j)$, where i and j indices correspond to vertical and horizontal coordinates, and z_{ij} are geopotential heights (which we treat as the geometric heights since the difference is not important in this study). The relationship between refractivity and common meteorological parameters can be found in,

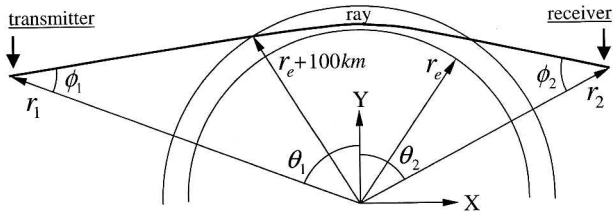

FIG. 5. Layout of ray tracing between transmitter and receiver.

for example, Thayer (1974). Next, ln ν was interpolated in the vertical direction by cubic splines onto the standard grid z_i, obtained by averaging z_{ij} over j.

Simulation of the bending angle as a function of impact parameter was performed by integration of ray equations in Cartesian coordinates, where they take simple form (Kravtsov and Orlov 1990)

$$d\mathbf{q}/d\tau = n\nabla n, \quad \mathbf{q} = d\mathbf{r}/d\tau, \tag{7}$$

where $\mathbf{r} = \{x, y\}$, $d\tau = dl/n$, by the fourth-order Runge–Kutta method (Press et al. 1992). For the integration of ray equations, generally, refractivity and its derivatives must be continuous functions. In practice, most important is continuity of the refractivity and its vertical derivative in the vicinity of ray TP. For each $\{x, y\}$ the corresponding $r = \sqrt{x^2 + y^2}$, $\theta = \arctan(x/y)$, and ν, $\nu_r' = \partial\nu/\partial r$, $\nu_\theta' = \partial\nu/\partial\theta$ were calculated and then converted to ν, $\nu_x' = \partial\nu/\partial x = x$, $\nu_r'/r - y\nu_\theta'/r^2$, $\nu_y' = \partial\nu/\partial y = y\nu_r'/r + x\nu_\theta'/r^2$. For the analytical model (4), all derivatives were calculated analytically. For the grid model, ν, ν_r', ν_θ' were calculated by applying log-spline interpolation in vertical and linear interpolation in horizontal direction, thus providing continuity of ν, ν_r'.

Geometry of ray tracing is shown in Fig. 5. The transmitter was fixed with respect to the atmosphere (this restriction simplifies calculations by not affecting results) at $r_1 = 26\,600$ km (typical for GPS), $\theta_1 = \text{const}$. Rays were started from transmitter at certain zenith angles ϕ_1 (the angle between ray and local vertical) with increment $\Delta\phi_1 = 1.5 \cdot 10^{-6}$ rad, then continued as straight lines until $r = r_e + 100$ km, then integrated through $n(x, y)$ until their altitude, again, became higher than 100 km, then again continued as straight lines until $r_2 = 7150$ km (receiver in LEO). At the end, the central angle of the receiver θ_2 and the zenith angle ϕ_2 were calculated for each ray. For a stationary transmitter, ϕ_2 is uniquely defined by an initial RO observable, Doppler frequency shift (Vorob'ev and Krasil'nikova 1994; Melbourne et al. 1994; Kursinski et al. 1997), while ϕ_1 is not known. Thus, in order to model real RO observations, both the impact parameter a and the bending angle α were calculated from only ϕ_2 under the assumption of spherical symmetry (by use of the Snell's law): $a = r_2 \sin\phi_2$ and $\alpha = \phi_2 + \arcsin(a/r_1) + (\theta_2 - \theta_1) - \pi$. Note that calculated α is different from the true angle between the vectors $\mathbf{q}_1$ and $\mathbf{q}_2$ at start and end of the ray. The central angle of the TP of the ray with a given α and a, also, was estimated under the assumption of the spherical symmetry: $\theta_{\text{tp}} = \theta_2 - \pi/2 + \phi_2 - \alpha/2$. Also note that thus estimated θ_{tp} is different from the true angle of tangent point (in fact, for nonspherical refractivity a ray may have several tangent points). We note that for a stationary transmitter, $\alpha(a)$ and $\theta_{\text{tp}}(a)$, in fact, do not depend on r_2 once the receiver is outside the atmosphere. The function $\alpha(a)$ was subject to Abel inversion for obtaining $n_{\text{ar}}(r)$:

$$\pi \ln n_{\text{ar}}(\rho) = \int_\rho^{r_e+100\text{km}} \frac{\alpha(a)}{\sqrt{a^2 - \rho^2}}\, da$$

$$\simeq \sum_i \frac{1}{\sqrt{a_i + \rho}} \int_{a_i}^{a_{i+1}} \frac{\alpha_i + \alpha_i'(a - a_i)}{\sqrt{a - \rho}}\, da = 2\sum_i \frac{\sqrt{a - \rho}[\alpha_i - \alpha_i'(a_i - \rho) + \alpha_i'(a - \rho)/3]|_{a=a_i}^{a=a_{i+1}}}{\sqrt{a_i + \rho}}, \tag{8}$$

where: $r = \rho/n_{\text{ar}}(\rho)$, the finite-difference approximation for the derivative is $\alpha_i' = (\alpha_{i+1} - \alpha_i)/(a_{i+1} - a_i)$ and decomposition of the denominator by setting $a + \rho = a_i + \rho$ at each integration step simplifies the calculation by preserving sufficient accuracy.

For integration of the excess phase path, when modeling the nonlocal refractivity, by (2)–(3), we apply the same interpolation of the 2D refractivity as for the ray tracing (see above). For integration of the excess phase path, when modeling it as the observable, we apply bilinear interpolation. Although this interpolation is coarse, its errors are canceled, to a considerable extent, when modeling S from $\upsilon_{\text{ar}}(r)$ and from $\upsilon(x, y)$, when the same finite-difference representation is applied (see section 2b). Similarly, trilinear interpolation can be applied for numerical implementation of the observation operator when assimilating real RO data.

In the lowest part of the troposphere (below ~2 km) the used high-resolution atmospheric model sometimes results in multipath propagation. In principle, it is possible to account for the multipath propagation in simulations by resorting rays after the ray tracing according

to increasing value of the impact parameter a. However, accurate resolving of the single-valued function $\alpha(a)$ in this case requires significant reduction of both the $\Delta\phi_1$ and the step for numerical integration of (7). In this study we simply stopped using data below the point where multipath was hit. When processing real RO data, the multipath is effectively resolved; that is, a single-valued function $\alpha(a)$ is reconstructed by applying radioholographic methods for complex received RO signal (Gorbunov 2002; Jensen et al. 2003) and then subject to Abel inversion. However, in case of superrefraction, which most commonly occurs on top of the PBL (Sokolovskiy 2003) the $n_{ar}(r)$, and hence the $S_{obs}(r_{tp})$ or $S_{obs}(a)$ modeled from the $n_{ar}(r)$, will be negatively biased below the superrefraction layer.

5. Results of the simulations

Figures 3 and 4 demonstrate 1D observation error profiles (differences between the "true" and the modeled observables) for the 2D refractivity model (4) and certain positions of the satellites. To access the accuracy of the nonlocal linear modeling of observables with the high-resolution WRF model, we simulate a very dense set of occultations (300 occultations for each case) shifted by a small increment in the horizontal direction, and then plot the errors as the 2D functions of the horizontal distance $r_e\theta$ and height z. Such a dense set of simultaneous occultations (not possible in practice) allows visualization of the spatial structure of errors.

Figure 6a shows the 2D cross section of the 3D WRF refractivity in a vertical plane cutting across the atmospheric front, which triggered strong convection uprising to high altitudes. The strong convection can be seen between 1000 and 1400 km in the horizontal distance mark. The date and time of the case and the geographic coordinates of the edges of the cross section are indicated on top of Fig. 6a. Figure 6b shows fractional difference between the local refractivity at the estimated ray TP and the AR refractivity. In some regions, especially in the region of strong convection, this difference is very large, about ±10%. Figure 6c shows the fractional difference between the nonlocal refractivity, modeled by use of straight lines, and the AR refractivity. This difference is substantially (approximately by one order of magnitude) smaller than the difference in Fig. 6b, thus demonstrating the advantage of modeling of the AR refractivity as the nonlocal refractivity. Figures 6d and 6e show fractional differences between the excess phase paths modeled by use of the 2D cross section of the 3D WRF and 1D AR refractivities. Figure 6d corresponds to the use of straight lines and Fig. 6e to the curved lines, given by (5) with the r_c given by

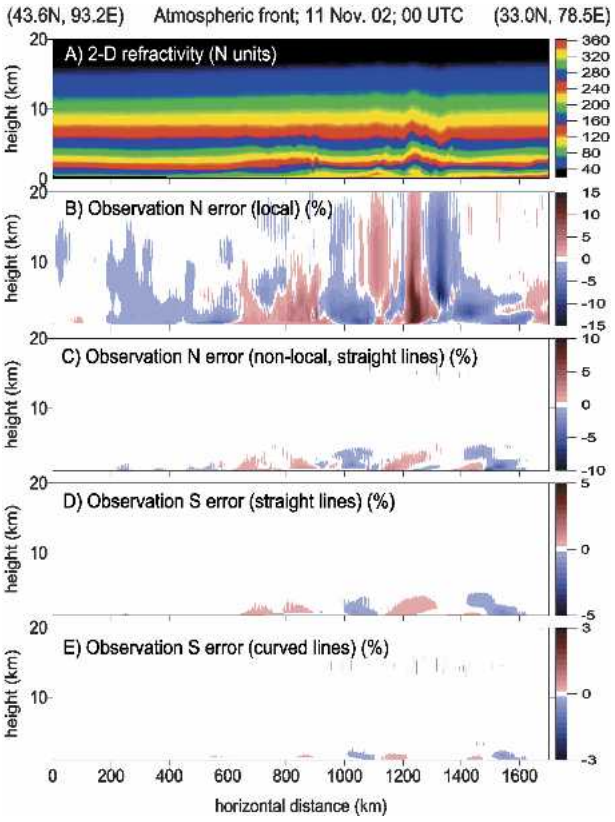

FIG. 6. (a) Two-dimensional refractivity in vertical plane across the atmospheric front. Fractional observation errors of modeling of (b), (c) the AR refractivity and of (d), (e) the excess phase path (for details see text).

(7), for the integration of the excess phase path. As seen, the use of the excess phase path as the observable results in further reduction of the modeling errors to the subpercentage level. The use of curved rays (Fig. 6e) results in smaller modeling errors compared to straight-line rays (Fig. 6d), as was expected from Fig. 4 [note that the range of color is decreasing from (d) to (e)].

Figure 7 shows the same as Fig. 6, but for the case of Hurricane Isabel. The "eye" of the hurricane can be seen between 800 and 900 km in the horizontal distance mark. In some regions, especially in the eye of the hurricane, the difference between the AR and the local refractivities is very large, about ±10%. Again, modeling of the nonlocal refractivity results in reduction of the observation errors, compared to the use of the local refractivity, by approximately one order of magnitude. Further reduction of the observation errors is achieved by modeling of the excess phase path and by use of the curved models or rays.

While comparing fractional modeling errors of different observables, for example, in this study the local

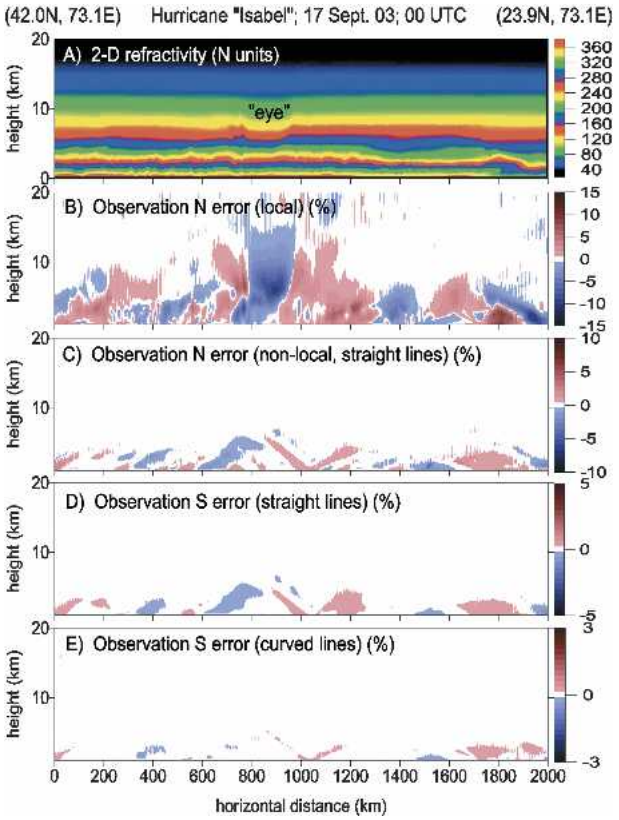

FIG. 7. Same as in Fig. 6, but for the case of Hurricane Isabel.

refractivity, the nonlocal refractivity, and the phase, it is necessary to take into account their natural (weather related) fractional variability whose magnitude is different for each observable. For coarse evaluation of the variability we interpolated each of those multiple vertical profiles used for obtaining 2D structures in Figs. 6 and 7 on a standard vertical grid, then calculated mean for each height (by averaging in horizontal direction) and rms deviation around the mean. The results are shown in Fig. 8 in fractional representation (normalize by the mean of the corresponding observable at each height). Solid lines show rms deviations of the observables and dashed lines their rms modeling errors: 1—of the local refractivity, 2—of the nonlocal refractivity, and 3—of the phase. Naturally, the shape of curves in Fig. 8 depends on the atmospheric state used for the modeling, but the following features are common in case of strong horizontal N gradients. The rms error of local refractivity is smaller, but not significantly, than its rms deviation. The rms errors of the nonlocal refractivity and the phase are significantly, by about one order of magnitude, smaller than their rms deviations. Both the rms deviation and the rms error of the phase are smaller (about 2 times) than those of the nonlocal refractivity. Thus both the nonlocal refractivity and the phase allow us to effectively account for the horizontal N gradients.

It is important to realize that the nonlocal linear modeling of RO observables, although it allows us to significantly reduce the modeling errors compared to the use of local refractivity, does not mean that those observables, by themselves, are resolving small-scale horizontal structures of refractivity. Information about such structures is convolved in the nonlocal observables. Being assimilated, these observables result in a constraint, which may aid a high-resolution NWP model to resolve the small-scale structures.

Nonlocal linear modeling of RO observables, such as

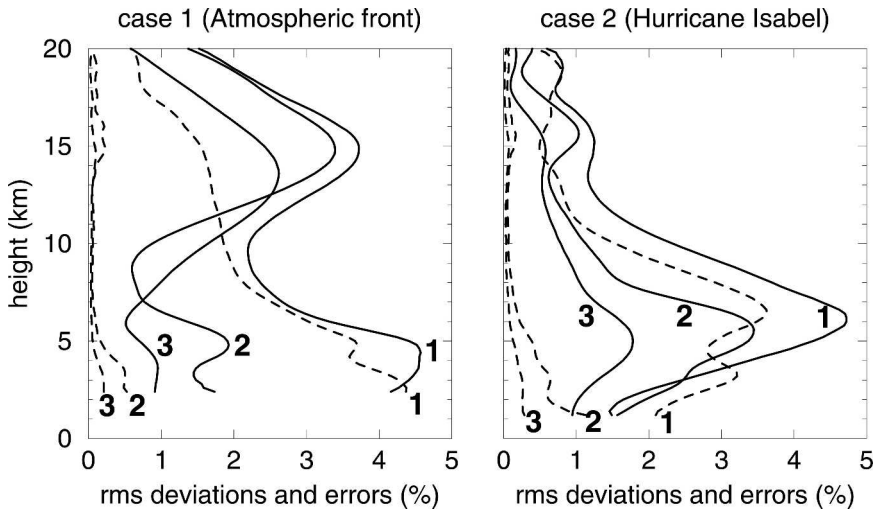

FIG. 8. Solid lines show fractional rms deviations, and dashed lines show fractional rms modeling errors of the observables: 1—of the local refractivity, 2—of the nonlocal refractivity, and 3—of the phase.

the refractivity and the phase, results in significant reduction of the fractional modeling errors, compared to the errors of modeling of the AR refractivity as the local refractivity. However, it must be noted that in most cases RO observations provide higher vertical resolution than NWP models. Direct assimilation of RO observables may result in aliasing of small vertical scales (not reproduced by models) into larger scales (Kursinski et al. 2000; Kuo et al. 2000, 2004). This can be treated as the representativeness error related to insufficient vertical resolution of most NWP models. To reduce this error, the AR refractivity must be subject to filtering and downsampling with bandwidth and discretization variable with height, in order to make them consistent with those of the NWP model.

The representativeness errors related to finite horizontal resolution of an NWP model manifest themselves in different ways for local and nonlocal observables. Here we demonstrate the effect of horizontal resolution of an atmospheric model on the representativeness error, when modeling the AR refractivity as local and nonlocal (by use of straight lines) refractivities. For this purpose we consider the AR refractivity profiles, simulated with the original high-resolution NWP model, as the "true" observables. However, when modeling the local and nonlocal refractivities we degrade the original horizontal resolution of the model by applying sliding averaging in the horizontal direction. The results, obtained in the case of Hurricane Isabel, are shown in Fig. 9. Panels (a) show the 2D refractivity field horizontally smoothed with 100-, 200-, 300-, 400-, and 500-km scale. For each smoothing scale, (b) and (c) show fractional observation errors when modeling the AR refractivity as local and nonlocal (by use of straight lines).

It can be seen that degradation of the horizontal resolution of the model, at first, results in reduction of the observation error of the local refractivity. This error achieves minimum at about 300-km horizontal resolution of the model and then increases again. We note that 300 km is approximately one-half of the horizontal resolution of RO method commonly defined as $2\sqrt{2r_eH} \simeq 600$ km, where H is the vertical refractivity scale (Melbourne et al. 1994; Kursinski et al. 1997; Ahmad 1998). When the horizontal resolution of an NWP model is degraded beyond $\sqrt{2r_eH}$, then the observation error increases again, but then this error is due to insufficient resolution of the atmospheric model. Thus the observation error of the local refractivity is driven by the observation modeling errors for atmospheric models with high horizontal resolution and by the model representativeness errors for low-resolution NWP models. The observation error of the nonlocal refractivity increases with degrading horizontal resolution of an atmospheric model, being driven by only representativeness error of the model. When the horizontal resolution of an NWP model is $\sqrt{2r_eH}$, the observation errors of local and nonlocal refractivities become close. In the particular case of infinitely poor horizontal resolution (spherical symmetry) the local and nonlocal refractivities (and thus their errors) are strictly equal, as it follows from (2) and (3).

6. Conclusions

Simulations with the high-resolution WRF model performed in this study demonstrate that nonlocal linear modeling of the AR refractivity allows us to substantially reduce the observation errors (in this study we do not consider measurement errors) compared to the errors of modeling of the AR refractivity as local. For the weather model with 4-km horizontal resolution, and extreme cases selected for this study, the reduction of the observation errors, in regions with large horizontal gradients, was about one order of magnitude.

We introduced the new observable, which is the phase integrated along certain trajectories (models of rays) through the AR refractivity. Modeling of this observable consists of integration of the phase along exactly the same trajectories through the NWP refractivity. The phase operator is very simple in implementation and results in a smaller number of operations than the nonlocal refractivity, being applied iteratively. An arbitrary, even very crude, finite-difference approximation can be applied for numerical integration of the phase, but it is important that this approximation be the same for the AR refractivity and for the NWP model refractivity, thus resulting in significant cancellation of the modeling errors. With the high-resolution model used in this study, the observation errors of the excess phase were about 2 times smaller than those of the nonlocal refractivity (however, weather-related variability of the phase was also about 2 times smaller than that of the nonlocal refractivity).

An important feature of both the refractivity and the phase nonlocal linear operators is that they are applied below the top of an NWP model so that extrapolation of refractivity above the top is not needed. However, when approaching the top of an NWP model, the information about horizontal gradients vanishes in both nonlocal refractivity and the phase (the nonlocal refractivity converges to the local refractivity and the phase converges to zero at the top of the NWP model). Thus application of the nonlocal linear operators is advantageous (allowing us to effectively account for the horizontal gradients) at heights lower than the top of an NWP model by at least one vertical atmospheric scale.

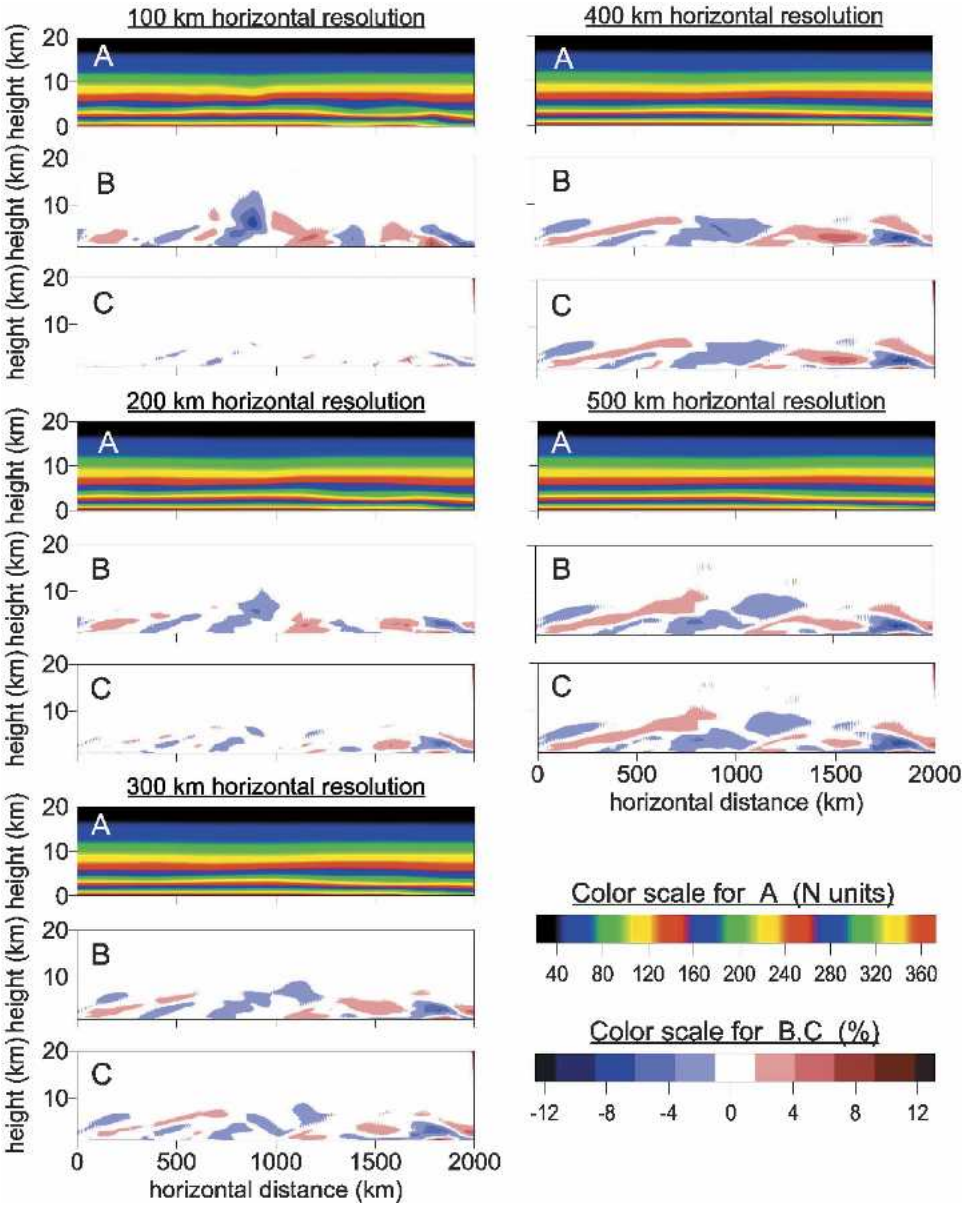

FIG. 9. (A panels) Two-dimensional model refractivity field (case Hurricane Isabel) smoothed horizontally with different scales. Fractional modeling errors of (B panels) local and (C panels) nonlocal refractivities for the different scales in the A panels.

Since generally the vertical resolution of RO is higher than of most of those of the NWP models, it is important to smooth and downsample the AR refractivity to make its vertical resolution and discretization consistent with those of the NWP model. This will reduce the representativeness error associated with vertical discretization of the NWP model.

Reduction of the observation errors, when modeling the nonlocal observables instead of the local refractivity, increases with increasing horizontal resolution of an NWP model. The use of the nonlocal linear observables is most important for high-resolution weather models (with the horizontal resolution < 100 km) where it allows us to effectively account for horizontal refractivity gradients. In low-resolution models (with the horizontal resolution of about 300 km or more) the horizontal refractivity structures are averaged comparably or stronger than they are convolved in RO observation. For such models, the use of nonlocal observables does not result in reduction of the observation errors, which are dominated by model representativeness errors. For high-resolution NWP models, significant reduction of

the observation errors, when using the nonlocal observables instead of the local refractivity, does not mean that those observables, by themselves, provide information on small-scale horizontal structures of refractivity. This information is contained in convolved form, that is, in the form of a constraint that may aid a high-resolution NWP model to resolve the small-scale structures.

Multipath propagation in the lower troposphere does not impede the use of the AR refractivity for modeling of nonlocal observables such as the phase. However, in the case of the superrefraction, both the AR refractivity and the modeled phase will be negatively biased below the layer.

Simulations in this study were performed for vertical occultation geometry. Nonlocal linear modeling of observables on the base of AR refractivity for occultations with big horizontal smears of TP in the transverse direction must be evaluated in an additional study.

Acknowledgments. This work was supported by the National Science Foundation (NSF) as part of development of the Constellation Observing System for Meteorology Ionosphere and Climate (COSMIC) Data Analysis and Archiving Center (CDAAC) at UCAR, and NSF Office of Polar Programs (OPP) Grant NSF OPP-0230361, under the Cooperative Agreement ATM-9732665, the Office of Naval Research, Code 322MM, the National Aeronautics and Space Administration, through Grant NAG 5-9518 to Ohio State University and UCAR. We are grateful to Stig Syndergaard for useful discussions of the subject, to Shu-Hua Chen for suggesting appropriate references, and to anonymous referees for reading and commenting on the paper.

REFERENCES

Ahmad, B., 1998: Accuracy and resolution of atmospheric profiles obtained from radio occultation measurements. Scientific Rep. DPD811-1988-1, Center for Radar Astronomy, Stanford, CA, 123 pp.

——, and G. L. Tyler, 1998: The two-dimensional resolution kernel associated with retrieval of ionospheric and atmospheric refractivity profiles by Abelian inversion of radio occultation phase data. *Radio Sci.,* **33,** 129–142.

——, and ——, 1999: Systematic errors in atmospheric profiles obtained from Abelian inversion of radio occultation data: Effects of large-scale horizontal gradients. *J. Geophys. Res.,* **104,** 3971–3992.

Anthes, R. A., C. Rocken, and Y.-H. Kuo, 2000: Application of COSMIC to meteorology and climate. *Terr. Atmos. Oceanic Sci.,* **11** (1), 115–156.

Chen, S.-H., and W.-Y. Sun, 2002: A one dimensional time-dependent cloud model. *J. Meteor. Soc. Japan,* **80,** 99–118.

Eyre, J. R., 1994: Assimilation of radio occultation measurements into a numerical weather prediction system. European Centre for Medium-Range Weather Forecasts, Tech. Memo. 199, 34 pp.

Feng, D. D., and B. M. Herman, 1999: Remotely sensing the earth's atmosphere using the global positioning system (GPS). *J. Atmos. Oceanic Technol.,* **16,** 989–1002.

Gorbunov, M. E., 1990: Solution of inverse problems of remote atmospheric refractometry on limb paths. *Izv. Atmos. Oceanic Phys.,* **26,** 86–91.

——, 2002: Canonical transform method for processing radio occultation data in the lower troposphere. *Radio Sci.,* **37,** 1076, doi:10.1029/2000RS002592.

——, and S. V. Sokolovskiy, 1993: Remote sensing of refractivity from space for global observation of atmospheric parameters. Max Planck Institute for Meteorology Rep. 119, 58 pp.

——, and L. Kornblueh, 2003: Principles of variational assimilation of GNSS radio occultation data. Max Planck Institute for Meteorology Rep. 350, 34 pp.

——, S. V. Sokolovskiy, and L. Bengtsson, 1996: Space refractive tomography of the atmosphere: Modeling of direct and inverse problems. Max Planck Institute for Meteorology Rep. 210, 59 pp.

Gurvich, A. S., and S. V. Sokolovsky, 1985: Reconstruction of a pressure field by remote refractometry from space. *Izv. Atmos. Oceanic Phys.,* **21,** 7–13.

——, and T. G. Krasil'nikova, 1987: Navigation satellites for radio sensing of the earth's atmosphere. *Sov. J. Remote Sens.,* **7,** 89–93.

Hajj, G. A., E. R. Kursinski, L. J. Romans, W. I. Bertiger, and S. S. Leroy, 2002: A technical description of atmospheric sounding by GPS occultation. *J. Atmos. Sol.-Terr. Phys.,* **64,** 451–469.

Hardy, E. R., D. P. Hinson, G. L. Tyler, and E. R. Kursinski, 1992: Atmospheric profiles from active space-based radio measurements. Preprints, *Sixth Conf. on Satellite Meteorology and Oceanography,* Atlanta, GA, Amer. Meteor. Soc., 420–423.

Hocke, K., 1997: Inversion of GPS meteorology data. *Ann. Geophys.,* **15,** 443–450.

Jensen, A. S., M. S. Lohmann, H.-H. Benzon, and A. S. Nielsen, 2003: Full spectrum inversion of radio occultation signals. *Radio Sci.,* **38,** 1040, doi:10.1029/2002RS002763.

Kravtsov, Yu. A., and Yu. I. Orlov, 1990: Geometrical optics of inhomogeneous media. Springer-Verlag, 216 pp.

Kuo, Y.-H., S. V. Sokolovskiy, R. A. Anthes, and F. Vandenberghe, 2000: Assimilation of GPS radio occultation data for numerical weather prediction. *Terr. Atmos. Oceanic Sci.,* **11** (1), 157–186.

——, T.-K. Wee, S. Sokolovskiy, C. Rocken, W. Schreiner, D. Hunt, and R. A. Anthes, 2004: Inversion and error estimation of GPS radio occultation data. *J. Meteor. Soc. Japan,* **82B,** 507–531.

Kursinski, E. R., G. A. Hajj, J. T. Schofield, R. P. Linfield, and K. R. Hardy, 1997: Observing earth's atmosphere with radio occultation measurements using the global positioning system. *J. Geophys. Res.,* **102** (D19), 23 429–23 465.

——, ——, S. S. Leroy, and B. M. Herman, 2000: The GPS radio occultation technique. *Terr. Atmos. Oceanic Sci.,* **11** (1), 235–272.

Lin, Y.-L., R. D. Farley, and H. D. Orville, 1983: Bulk parameterization of the snow field in a cloud model. *J. Climate Appl. Meteor.,* **22,** 1065–1092.

Liu, H., and X. Zou, 2003: Improvements to a GPS radio occultation ray-tracing model and their impacts on assimilation of

bending angle. *J. Geophys. Res.,* **108,** 4548, doi:10.1029/2002JD003160.

——, ——, H. Shao, R. A. Anthes, J. C. Chang, J.-H. Tseng, and B. Wang, 2001: Impact of 837 bending angle profiles on assimilation and forecasts for the period June 20–30, 1995. *J. Geophys. Res.,* **106** (D23), 31 771–31 786.

Marquardt, C., J. Eyre, S. Healy, A. Jupp, and D. Offiler, 2003: Use of GPS radio occultation data in meteorological services. U.K. Met Office Forecast Research Tech. Rep. 403, 9 pp.

Melbourne, W. G., and Coauthors, 1994: The application of spaceborne GPS to atmospheric limb sounding and global change monitoring. JPL Publication 94-18, 147 pp.

Michalakes, J., S. Chen, J. Dudhia, J. Klemp, J. Middlecoff, and W. Skamarock, 2001: Development of a next generation regional weather research and forecast model. *Developments in Teracomputing: Proceedings of the Ninth ECMWF Workshop on the Use of High Performance Computing in Meteorology*, W. Zwieflhofer and N. Kreitz, Eds., World Scientific, 269–276.

Poli, P., 2004: Effects of horizontal gradients on GPS radio occultation observation operators. II: A Fast Atmospheric Refractivity Gradient Operator (FARGO). *Quart. J. Roy. Meteor. Soc.,* **130,** doi:10.1256/qj.03.229.

——, and J. Joiner, 2004: Effects of horizontal gradients on GPS radio occultation observation operators. I: Ray tracing. *Quart. J. Roy. Meteor. Soc.,* **130,** doi:10.1256/qj.03.228.

——, ——, and E. R. Kursinski, 2002: 1DVAR analysis of temperature and humidity using GPS radio occultation refractivity data. *J. Geophys. Res.,* **107,** 4448, doi:10.1029/2001JD000935.

Press, W. H., S. A. Teukolsky, W. T. Vetterling, and B. P. Flannery, 1992: *Numerical Recipes in Fortran 77.* Cambridge University Press, 933 pp.

Rocken, C., and Coauthors, 1997: Analysis and validation of GPS/MET data in the neutral atmosphere. *J. Geophys. Res.,* **102** (D25), 29 849–29 866.

Skamarock, W. C., J. B. Klemp, and J. Dudhia, 2001: Prototypes for the Weather Research and Forecasting Model (WRF). Preprints, *Ninth Conf. on Mesoscale Processes,* Fort Lauderdale, FL, Amer. Meteor. Soc., J11–J15.

Sokolovsky, S. V., 1986: Possibility for remote refractometric sensing of the atmosphere using FGGE (First Global GARP Experiment) data: Numerical experiment. *Izv. Atmos. Oceanic Phys.,* **22,** 691–693.

——, 2003: Effect of superrefraction on inversions of radio occultation signals in the lower toposphere. *Radio Sci.,* **38,** 1058, doi:10.1029/2002RS002728.

Steiner, A. K., G. Kirchengast, and H. P. Ladreiter, 1999: Inversion, error analysis, and validation of GPS/MET occultation data. *Ann. Geophys.,* **17,** 122–138.

Syndergaard, S., 1999: Retrieval analysis and methodologies in atmospheric limb sounding using GNSS radio occultation technique. Danish Meteorological Institute Scientific Rep. 99–6, Copenhagen, Denmark, 75 pp.

——, D. Flittner, R. Kursinski, and B. Herman, 2003: Simulating the influence of horizontal gradients on refractivity profiles from radio occultations. *Proc. Fourth Oersted Int. Science Team Conf. (OIST-4),* Copenhagen, Denmark, Danish Meteorological Institute, 245–250.

——, ——, ——, E. M. Lane, and D. E. Flittner, 2005: A refractive index mapping operator for assimilation of occultation data. *Mon. Wea. Rev.,* in press.

Thayer, G. D., 1974: An improved equation for the radio refractive index of air. *Radio Sci.,* **9,** 803–807.

Vorob'ev, V. V., and T. G. Krasil'nikova, 1994: Estimation of the accuracy of the atmospheric refractive index recovery from Doppler shift measurements at frequencies used in the NAVSTAR system. *Izv. Atmos. Oceanic Phys.,* **29,** 602–609.

Wickert, J., and Coauthors, 2001: Atmosphere sounding by GPS radio occultation: First results from CHAMP. *Geophys. Res. Lett.,* **28,** 3263–3266.

Yunck, T. P., G. F. Lindall, and C.-H. Liu, 1988: The role of GPS in precise earth observation. *Proc. Position Location and Navigation Symp. (PLANS 88),* Orlando, FL, IEEE, 251–258.

——, C.-H. Liu, and R. Ware, 2000: A history of GPS sounding. *Terr. Atmos. Oceanic Sci.,* **11,** 1–20.

Zou, X., Y.-H. Kuo, and Y.-R. Guo, 1995: Assimilation of atmospheric radio refractivity using a nonhydrostatic adjoint model. *Mon. Wea. Rev.,* **123,** 2229–2249.

——, and Coauthors, 1999: A ray-tracing operator and its adjoint for the use of GPS/MET refraction angle measurements. *J. Geophys. Res.,* **104,** 22 301–22 318.

——, B. Wang, H. Liu, R. A. Anthes, T. Matsumura, and Y. J. Zhu, 2000: Use of GPS/MET refraction angles in three-dimensional variational analysis. *Quart. J. Roy. Meteor. Soc.,* **126,** 3013–3040.